npj computational materials

www.nature.com/npjcompumats

ARTICLE OPEN

Check for updates

Thermodynamical and topological properties of metastable Fe_3Sn

Chen Shen[1,3], Ilias Samathrakis[1,3], Kun Hu[1,2✉], Harish K. Singh[1], Nuno Fortunato[1], Huashan Liu[2], Oliver Gutfleisch[1] and Hongbin Zhang[1✉]

The Fe–Sn-based kagome compounds attract intensive attention due to its attractive topological transport and rich magnetic properties. Combining experimental data, first-principles calculations, and Calphad assessment, thermodynamic and topological transport properties of the Fe–Sn system were investigated. Density functional theory (DFT) calculations were performed to evaluate the intermetallics' finite-temperature heat capacity (C_p). A consistent thermodynamic assessment of the Fe–Sn phase diagram was achieved by using the experimental and DFT results, together with all available data from previous publications. Here, we report that the metastable phase Fe_3Sn was introduced into the current metastable phase diagram, and corrected phase locations of Fe_5Sn_3 and Fe_3Sn_2 under the newly measured corrected temperature ranges. Furthermore, the anomalous Hall conductivity and anomalous Nernst conductivity of Fe_3Sn were calculated, with magnetization directions and doping considered as perturbations to tune such transport properties. It was observed that the enhanced anomalous Hall and Nernst conductivities originate from the combination of nodal lines and small gap areas that can be tuned by doping Mn at Fe sites and varying magnetization direction.

npj Computational Materials (2022)8:248 ; https://doi.org/10.1038/s41524-022-00917-1

INTRODUCTION

The kagome lattice is a 2D network of corner-sharing triangles that has been intensively investigated the last years. Due to its unusual geometry, it offers a playground to study interesting physics, including frustrated, correlated[1,2], exotic topological quantum[1–16], topological Chern[17], insulating and Weyl semimetal[13,18] phases, originating from the interplay between magnetism and electronic topology. In fact, the kagome lattice has been realized in several materials including metal stannides, germannides[19,20] as well as T_mX_n compounds with T = Mn, Fe, Co, X = Sn, Ge (m: n = 3:1, 3:2, 1:1)[21]. Recent studies demonstrated that Fe–Sn-based kagome compounds exhibiting interesting properties, such as large magnetic tunability[1]. Furthermore, they can host Dirac fermions and flat bands, as found in Fe_3Sn_2[22,23] and FeSn[21,24]. The existence of spin degenerate band touching points was linked to the generation of several interesting phenomena. Specifically, the anomalous Hall effect (AHE) results in a transverse spin-polarized charge current (charge current and spin current due to the imbalance of spin up and spin down electrons in ferromagnets) in response to a longitudinal charge current, in the absence of an external magnetic field[25–29]. This applies also to its thermal counterpart, the anomalous Nernst effect (ANE), in which the external stimuli is replaced by a thermal gradient[30] as well as the Seebeck effect[31].

Interestingly, the Fe–Sn-based intermetallics compounds not only exhibit attractive topological transport properties, but also show rich magnetic properties. In our previous studies[32,33], a DFT screening of the Fe–Sn phase diagram was used to identify Fe–Sn-based phases with the potential to be stabilized upon alloying, and their magnetization and magnetocrystalline anisotropy were evaluated. The results revealed that a strong anisotropy as observed in Fe_3Sn may also be found in other Fe–Sn-based phases, having high potential to be used as hard magnetic materials. Meanwhile, we applied the reactive crucible melting (RCM) approach to the Fe–Sn binary system, and observed three metastable intermetallic compounds, namely Fe_3Sn, Fe_5Sn_3, Fe_3Sn_2, which are ferromagnetic and exist between 873 K and 1173 K. We found that such metastable phases can be synthesized using the RCM method at specific temperature ranges. What's more, phase diagram of the Fe–Sn system reported in the literature[19,34,35] has mentioned that the Fe_3Sn was considered to be a metastable phase, and presented the relevant so-called metastable composition range and phase relations. According to Fayyazi's[32] work, the reactive crucible reproduced the corresponding phase relations as in the bulk samples at 998 K (α-Fe, Fe_3Sn_2, FeSn, and Sn) and 1023 K (Fe_3Sn_2, Fe_3Sn, and FeSn), of which Fe_3Sn can only be stabilized between 1023–1098 K during a non-equilibrium process as a metastable phase but disappears at 1123 K due to the presence of Fe_5Sn_3 phase. Accordingly, adding more details to the phase diagram of the metastable Fe_3Sn phase, with the discovered temperature range based on the reported phase diagram is of great significance. Therefore, to further explore the interesting properties of metastable Fe–Sn phases, it is important to understand the phase diagram and thermodynamical properties of the Fe–Sn system.

In this work, we adopted our new measurements[32,33] on the equilibria states of Fe_3Sn, Fe_5Sn_3, Fe_3Sn_2, combined with the thermodynamic properties of such intermetallic phases obtained based on first-principles calculations. A consistent thermodynamic assessment of the Fe–Sn system was then developed based on all available experimental and first-principles results. Furthermore, the AHC and ANC of Fe_3Sn were calculated and its dependence on the magnetization direction and doping were evaluated. We observed that there exist significant changes in AHC and ANC by

[1]School of Materials Science, Technical University Darmstadt, Otto-Berndt-Straße 3, Darmstadt 64287, Germany. [2]School of Materials Science and Engineering, Central South University, Lushan South Road 932, 410083 Changsha, China. [3]These authors contributed equally: Chen Shen, Ilias Samathrakis. ✉email: kh89jyni@tu-darmstadt.de; hzhang@tmm.tu-darmstadt.de

Table 1. Lattice parameters of intermetallics from first-principles calculations compared with experimental values.

Phases	Space group	Magnetism	Lattice parameters (Å)		k-point mesh	Refs.
			a	c		
Fe_3Sn	$P6_3/mmc$	FM	5.457	4.362		Ref. [58]
			5.461	4.347		Ref. [59]
			5.421	4.434		Ref. [60]
			5.440	4.372		Ref. [61]
			5.464	4.352		Ref. [19]
			5.475	4.307	10 × 10 × 12	This work
Fe_5Sn_3	$P6_3/mmc$	FM	4.223	5.253		Ref. [62]
Fe_3Sn_2	R-3 m	FM	5.344	19.845		Ref. [63]
			5.340	19.797		Ref. [19]
			5.315	19.703		Ref. [2]
			5.328	19.804	10 × 10 × 3	This work
FeSn	P6/mmm	AFM	5.307	4.445		Ref. [58]
			5.297	4.481		Ref. [64]
			5.288	4.420		Ref. [65]
			5.300	4.450		Ref. [66]
			5.298	4.448		Ref. [19]
			5.297	4.449		Ref. [67]
			5.299	4.449	10 × 10 × 10	This work
$FeSn_2$	I4/mcm	AFM	6.502	5.315		Ref. [68]
			6.539	5.325		Ref. [69]
			6.539	5.325		Ref. [70]
			6.542	5.326		Ref. [64]
			6.542	5.386		Ref. [65]
			6.536	5.323		Ref. [19]
			6.533	5.320		Ref. [71]
			6.545	5.326		Ref. [72]
			6.561	5.338	8 × 8 × 10	This work

tuning the Fermi energy via Mn-doping. Therefore, Fe_3Sn renders itself a promising candidate for new transverse thermoelectric devices with potential applications.

RESULTS AND DISCUSSION

Metastable phase diagram

Most end-members in the sublattice models are not stable and their thermodynamic data are impossible to be determined by experiments. First principles are hence performed to estimate the Gibbs energies of the compounds and end-members at finite temperatures. In order to benchmark the current DFT calculations, the calculated crystallographic information of phases in the binary Fe–Sn system are listed in Table 1, in comparison with the available experimental data. The calculated lattice parameters of the solid phases at 0 K are in good agreement with the experimental results at room temperature. As one can see, the differences between the theoretical and experimental lattice constants are within 0.5% for all the phases. Note that, in our earlier study[32,33], we showed, that the crystal structure of "Fe_5Sn_3" synthesized by the equilibrated alloy method, is not of the typically assumed hexagonal Laves structure (as shown in Table 1). We rather observed superstructure reflections in the powder XRD spectra that could not be explained by the hexagonal structure and we assigned to a modulated orthorhombic unit cell with lattice parameters of $a = 4.221$ Å, $b = 7.322$ Å, $c = 5.252$ Å. More details and explanations can be found in the refs. [32,33]. Hence, we used this structure to do phonon calculations. Furthermore, the calculated phonon bands of such phases are shown in Fig. 1. To prove the validity of the calculations, as shown in Fig. 1, the phonon dispersion of BCC-Fe is compared with the experimental data[36], presenting good agreement. Therefore, it is expected that the thermodynamical properties of the Fe–Sn intermetallic phases can also be accurately obtained based on DFT calculations. As shown in Fig. 1, no imaginary phonon modes exist for all the compounds, indicating that all the intermetallics are dynamically stable. And the quasi-harmonic approximation (QHA) can be used to calculate the thermodynamic properties.

The thermodynamic properties at finite temperatures are evaluated based on the Gibbs free energies specified in Eq. (5). And from the thermodynamical point of view, we can derive the Gibbs free energies from the heat capacity. To obtain the accurate heat capacity of the intermetallics, we firstly compare the calculated heat capacity of the BCC-Fe with the available experimental data[37], as shown in Fig. 2. Among that, the magnetic contribution to the heat capacity is analyzed following the theory of IHJ model[38,39] and further improved version by Xiong[40]:

$$C_{p_{\mathrm{mag}}} = R(\beta^* + 1)c(\tau). \quad (1)$$

Figure 2 shows isobaric heat capacity obtained from our DFT calculations. It can be observed that the lattice vibrations dominate other contributions to the heat capacity. Interestingly, the correction made by adding electronic and magnetic heat capacities shifted the result toward bigger values and after that calculations show an excellent agreement with the experimental

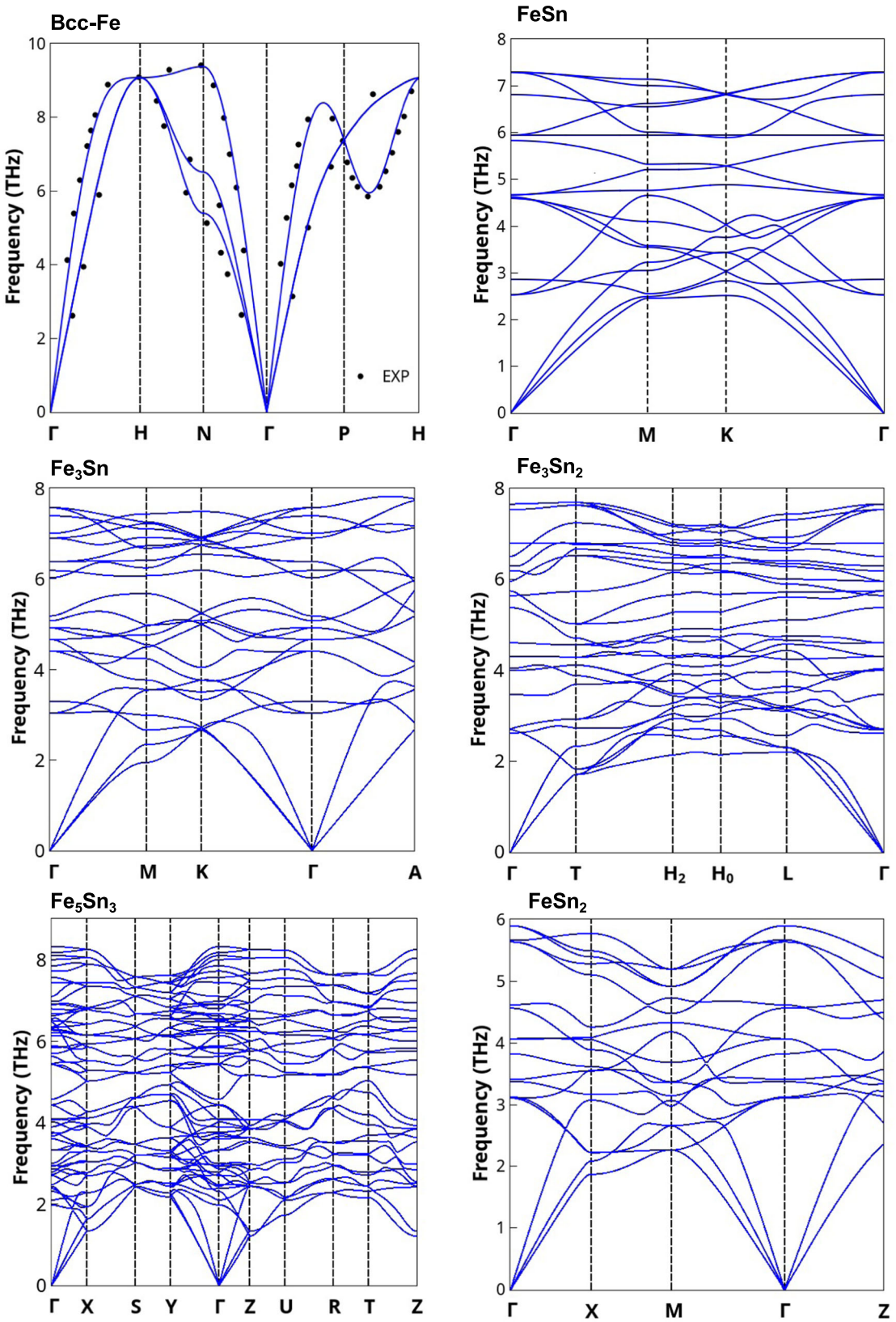

Fig. 1 Phonon dispersions of the pure elements and intermetallic phases in the Fe–Sn system. The black solid points represent the experimental data from ref. [37].

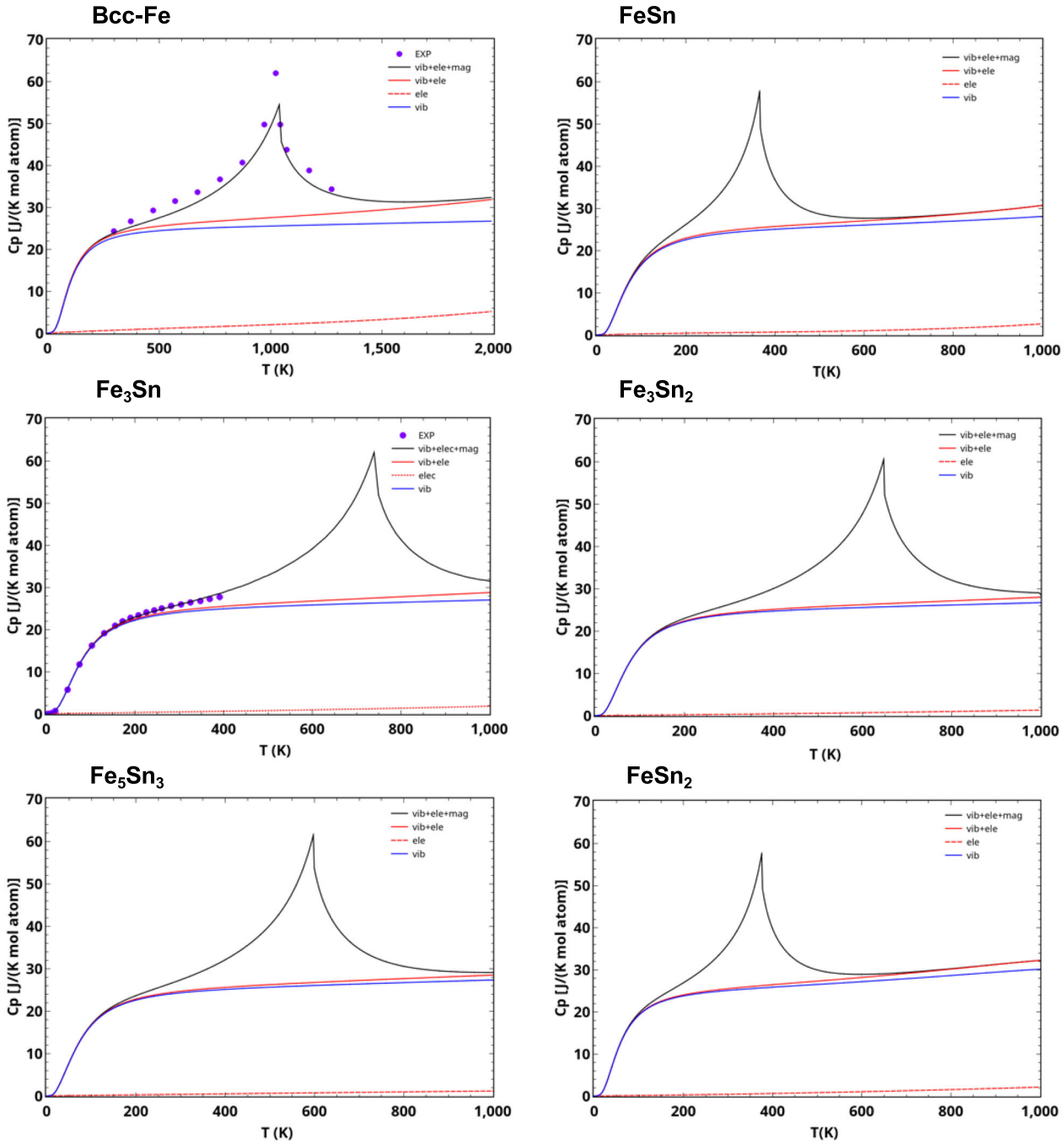

Fig. 2 Heat capacity of pure Fe and Sn from DFT calculations in comparison with the experiment data[37]. Those for all the intermetallics are also shown, experimental data of Fe_3Sn is obtained from our previous studies[32,33].

data[37]. More interestingly, the magnetic contribution to the heat capacity presents at the magnetic phase transition of BCC-Fe. These results prove the accuracy of the current methods and justify the following calculations for intermetallics. Using the same strategy, we calculate heat capacities of Fe_5Sn_3, Fe_3Sn_2, Fe_3Sn, $FeSn_2$, and FeSn at finite temperatures, as shown in Fig. 2, with the magnetic heat capacity evaluated using Inden model[39]. The heat capacity of Fe_3Sn shows a good consistency between our calculations and experiments at low temperature, which also confirms the accuracy of current theoretical results. We note that such good agreements are supported by considering the magnetic contributions in the magnetic system.

After getting the thermodynamical properties of intermetallics, we used CALPHAD method[41] to evaluate the thermodynamic model parameters of the Fe–Sn system, and the phase diagram and thermodynamic properties are calculated by Thermo-Calc[42]. Combining DFT and CALPHAD methods has already been successfully applied in different systems[43,44]. Supplementary Table 1 lists the modeled thermodynamic parameters of the Fe–Sn system. The calculated Fe–Sn phase diagram is presented in Fig. 3 along with the experimental data[32,45–56]. The comparison of the calculated temperatures and compositions of invariant reactions with experimental data[45–51] as well as results from previous thermodynamic assessments[35,57] are listed in Table 2.

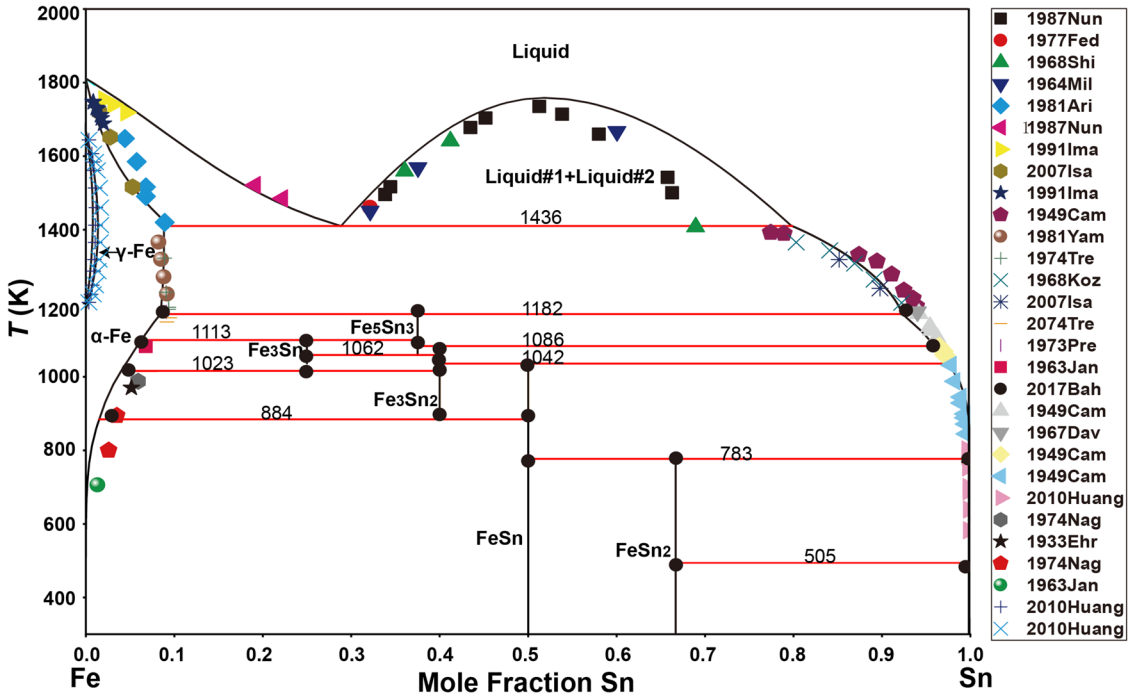

Fig. 3 The optimized Fe–Sn phase diagram based on our thermodynamic modeling. The points correspond to the different experimental data[32,45–56]. The red lines indicate the reaction temperatures between the different phases.

Using the reactive crucible melting (RCM) approach, it is found that 3 metastable intermetallic compounds, i.e., Fe_3Sn, Fe_5Sn_3, and Fe_3Sn_2, can be stabilized between 873 K and 1173 K. Furthermore, we are convinced that the phase diagram reported in the literature is inaccurate in the temperature interval 1023–1038 K and Fe_3Sn can exist at 1023 K. Thus, the metastable phase Fe_3Sn is introduced by considering the current accurate experimental results. Obviously, good agreement between the optimized and experimental (see Supplementary Figs. 1 and 2) shows the calculated thermodynamic properties of the compounds in current CALPHAD modeling, first-principles calculations, previous CALPHAD modeling and the experimental data. The calculated thermodynamic properties in this work are consistent with experimental data.

Topological transport properties

Our calculations demonstrate that Fe_3Sn exhibits the largest AHC among the Fe–Sn family. The calculated x-component of AHC (σ_x) for the equilibrium lattice parameters, with the magnetization direction along [100]-axis, reaches 757 S cm^{-1} at Fermi energy, as shown in Fig. 4a. This value is surprisingly large compared to the more than 3 times smaller value of 200 S cm^{-1} for Fe_3Sn_2[58]. In addition, Li et al. reported an experimentally measured value of 613 S cm^{-1} value as well as a calculated of 507 S cm^{-1} for Fe_5Sn_3[29], both being smaller than our value for Fe_3Sn. In addition, compared to other ferromagnetic kagome materials, it ranks among the largest reported, being larger than 380 S cm^{-1} of $LiMn_6Sn_6$[59] and 223 S cm^{-1} for $GdMn_6Sn_6$[60], but lower than the largest reported value of 1130 S cm^{-1} for $Co_3Sn_2S_2$[61]. Correspondingly, the ANC of Fe_3Sn, evaluated at $T = 300$ K, is also the largest among the Fe–Sn family. Specifically, it reaches −2.71 A m^{-1} K^{-1} (see Fig. 5b) being more than two times larger than the reported value of 1 A m^{-1} K^{-1} for Fe_3Sn_2[30]. Compared to the other kagome materials, Fe_3Sn exhibits a reasonably large ANC, being larger than 1.29 A m^{-1} K^{-1} and 0.20 A m^{-1} K^{-1} reported for $ZrMn_6Sn_6$ and $MgMn_6Sn_6$[62], but smaller than the largest reported value of 10 A m^{-1} K^{-1} for $Co_3Sn_2S_2$[63]. Compounds with large AHC and ANC values are promising candidates for transverse thermoelectric devices[64–67].

Symmetry plays a crucial role in determining the shape of the AHC and ANC tensors. AHC and ANC strongly depend on the Berry curvature which behaves as a pseudovector under the application of any symmetry operation[68,69] and transforms according to the formula

$$\mathbf{s\Omega}(\mathbf{r}) = \pm \det(\mathbf{D}(\mathbf{R}))\mathbf{D}(\mathbf{R})\mathbf{\Omega}(\mathbf{s}^{-1}\mathbf{r}), \tag{2}$$

where $\mathbf{\Omega}(\mathbf{r})$ denotes the pseudovector Berry curvature, $\mathbf{D}(\mathbf{R})$ the three-dimensional representation of a symmetry operation without the translation part and $\mathbf{s}$ an arbitrary symmetry operation. That is, the symmetry operations of the magnetic point group will govern the shape of the tensors. Particularly, the ferromagnetic Fe_3Sn belongs to the magnetic space groups $Cmc'm'$ (BNS: 63.463), $Cm'cm'$ (BNS: 63.464) and $P6_3/mm'c'$ (BNS: 194.270) for the magnetic moments of Fe atoms pointing along the [100]-, [010]- and [001]-axis, respectively. Hence the presence of the 2_x, 2_y and 2_z rotation axes for each of magnetic space groups transform the Berry curvature according to:

$$\begin{aligned}
&\text{For } 2_x \text{ with } M\|[100]\\
&\mathbf{\Omega}_x(k_x,-k_y,-k_z) = \mathbf{\Omega}_x(k_x,k_y,k_z)\\
&\mathbf{\Omega}_y(k_x,-k_y,-k_z) = -\mathbf{\Omega}_y(k_x,k_y,k_z)\\
&\mathbf{\Omega}_z(k_x,-k_y,-k_z) = -\mathbf{\Omega}_z(k_x,k_y,k_z).\\
&\text{For } 2_y \text{ with } M\|[010]\\
&\mathbf{\Omega}_x(-k_x,k_y,-k_z) = -\mathbf{\Omega}_x(k_x,k_y,k_z)\\
&\mathbf{\Omega}_y(-k_x,k_y,-k_z) = \mathbf{\Omega}_y(k_x,k_y,k_z)\\
&\mathbf{\Omega}_z(-k_x,k_y,-k_z) = -\mathbf{\Omega}_z(k_x,k_y,k_z).\\
&\text{For } 2_z \text{ with } M\|[001]\\
&\mathbf{\Omega}_x(-k_x,-k_y,k_z) = -\mathbf{\Omega}_x(k_x,k_y,k_z)\\
&\mathbf{\Omega}_y(-k_x,-k_y,k_z) = -\mathbf{\Omega}_y(k_x,k_y,k_z)\\
&\mathbf{\Omega}_z(-k_x,-k_y,k_z) = \mathbf{\Omega}_z(k_x,k_y,k_z).
\end{aligned} \tag{3}$$

The summation over the whole Brillouin zone forces σ_y and σ_z for the magnetization direction along the [100]-axis to vanish, and

Table 2. Summary of the invariant reactions in the Fe–Sn system.

Invariant reaction	Reaction type	Composition at % Sn			Temperature (K)	Refs.
Liquid#1 → BCC_A2 + Liquid#2	Eutectic	0.312	0.083	0.811	1395.9	Ref. [57]
					1381	Ref. [45]
					1404	Ref. [46]
					1403	Ref. [47]
					1403	Ref. [54]
					1407	Ref. [35]
					1413	Ref. [48]
	Eutectic	0.297	0.095	0.796	1436	This work
BCC_A2 + Liquid → Fe_5Sn_3	Peritectic	0.081	0.929	0.375	1174.1	Ref. [57]
					1166	Ref. [48]
					1168	Ref. [35]
					1183	Ref. [50]
					1183	Ref. [49]
	Peritectic	0.088	0.948	0.375	1182	This work
BCC_A2 + Fe_5Sn_3 → Fe_3Sn	Peritectic	0.064	0.375	0.250	1111	Ref. [32]
	Peritectic	0.062	0.375	0.250	1113	This work
Fe_5Sn_3 + Liquid → Fe_3Sn_2	Peritectic	0.375	0.967	0.400	1074.8	Ref. [57]
					1072	Ref. [51]
					1079	Ref. [50]
					1079	Ref. [49]
					1080	Ref. [35]
	Peritectic	0.375	0.979	0.400	1086	This work
Fe_5Sn_3 → Fe_3Sn + Fe_3Sn_2	Eutectoid	0.375	0.250	0.400	1055	Ref. [32]
	Eutectoid	0.375	0.250	0.400	1062	This work
Fe_3Sn_2 + Liquid → FeSn	Peritectic	0.400	0.980	0.500	1024.7	Ref. [57]
					1013	Ref. [47]
					1034	Ref. [35]
					1043	Ref. [50]
					1043	Ref. [49]
	Peritectic	0.400	0.979	0.500	1042	This work
Fe_3Sn → BCC_A2 + Fe_3Sn_2	Eutectoid	0.250	0.046	0.400	1023	Ref. [32]
	Eutectoid	0.250	0.046	0.400	1023	This work
Fe_3Sn_2 → BCC_A2 + FeSn	Eutectoid	0.400	0.017	0.500	874.9	Ref. [57]
					870	Ref. [51]
					873	Ref. [47]
					880	Ref. [50]
					880	Ref. [49]
					880	Ref. [35]
	Eutectoid	0.400	0.015	0.500	884	This work
FeSn + Liquid → $FeSn_2$	Peritectic	0.500	0.999	0.666	775.4	Ref. [57]
					769	Ref. [48]
					769	Ref. [45]
					769	Ref. [47]
					786	Ref. [49]
					786	Ref. [50]
					786	Ref. [35]
	Peritectic	0.500	0.999	0.666	783	This work
Liquid → $FeSn_2$ + BCT_A5	Eutectic	0.999	0.666	1.000	504.9	Ref. [57]
					501	Ref. [48]
					505	Ref. [49]
					505	Ref. [50]
					505	Ref. [35]
	Eutectic	0.999	0.666	1.000	505	This work

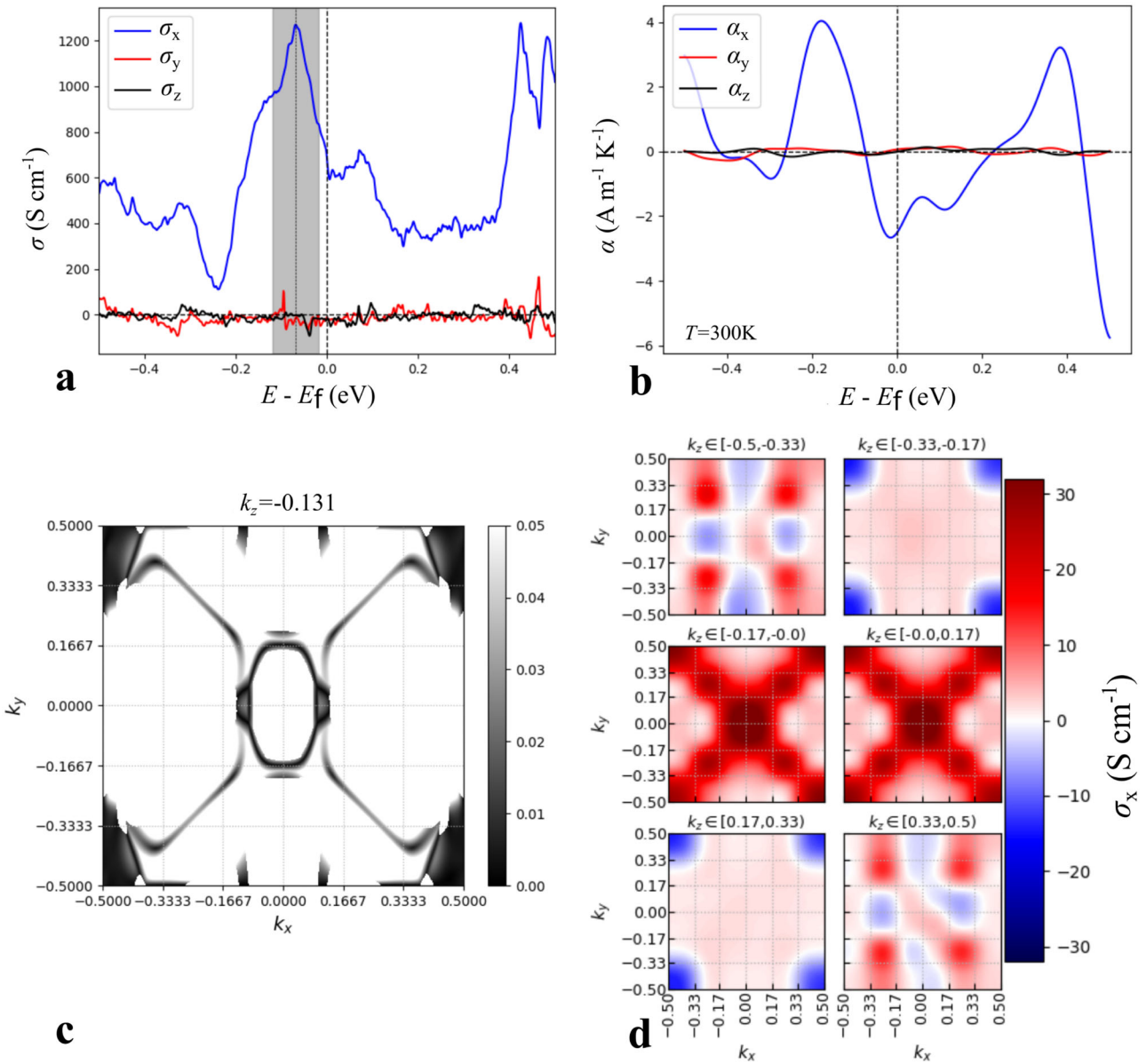

Fig. 4 Anomalous Hall/Nernst conductivities and Band gap of Fe_3Sn with *M*||[100]. **a** AHC components as a function of energy. **b** ANC components as a function of energy. **c** The band gap (eV) for a BZ-slice at $k_z = -0.131$ with its energies within the shaded energy range of part (**a**). **d** The distribution of the x-component ($\sigma_x = \sigma_{yz}$) of the full AHC at each part of the BZ.

equivalently σ_x and σ_z and σ_x and σ_y for the magnetization along [010] and [001], respectively. However, there is no such condition for σ_x, σ_y, and σ_z for magnetization direction along [100], [010], and [001] axes, respectively, and therefore they are allowed to have finite values.

AHC and ANC are proportional to the sum of the Berry curvature of the occupied bands, evaluated in the whole Brilouin zone (BZ), as defined in Eq (11). Since the Berry curvature depends on the energy difference between two adjacent bands, therefore it is expected that Weyl nodes as well as nodal lines, located close to the reference energy, contribute significantly to the total value, as shown in refs. [70,71] and confirmed for MnZn[62] and Mn_3PdN[72], respectively. Explicit band structure search reveals the presence of numerous Weyl nodes and nodal lines within the shaded energy range $[-0.118, -0.018]$ eV of Fig. 4a that are expected to contribute to the total AHC value. In order to identify the origin of the AHC contribution, we split the BZ into 216 cubes, within which the AHC is evaluated (see Fig. 4d). Since the major contribution originates from the diagonals, located within $k_z \in (-0.166, 0.000)$ (and $k_z \in (0.000, 0.166)$), as illustrated in Fig. 4d, it is fruitful to investigate the band gap within this k_z range. Taking as an example the $k_z = -0.131$ plane, we plot the difference of the two involved bands as a black and white plot where the black areas correspond to small gap regions whereas white areas to large gap regions (see Fig. 4c). The shape of the gap plot is in complete agreement with the distribution of the AHC within the specified area, demonstrating that small gap regions similar to those within the square $k_x, k_y \in (0.333, 0.500)$ of Fig. 4c, contribute dominantly to the total AHC value.

Interesting topological transport properties can arise away from the charge-neutral point. One important observation is that the AHC curve of Fe_3Sn exhibits a sharp peak of 1308 S cm^{-1} located at 60 meV below the Fermi level, as shown in Fig. 4. Therefore, an interesting question is whether tuning

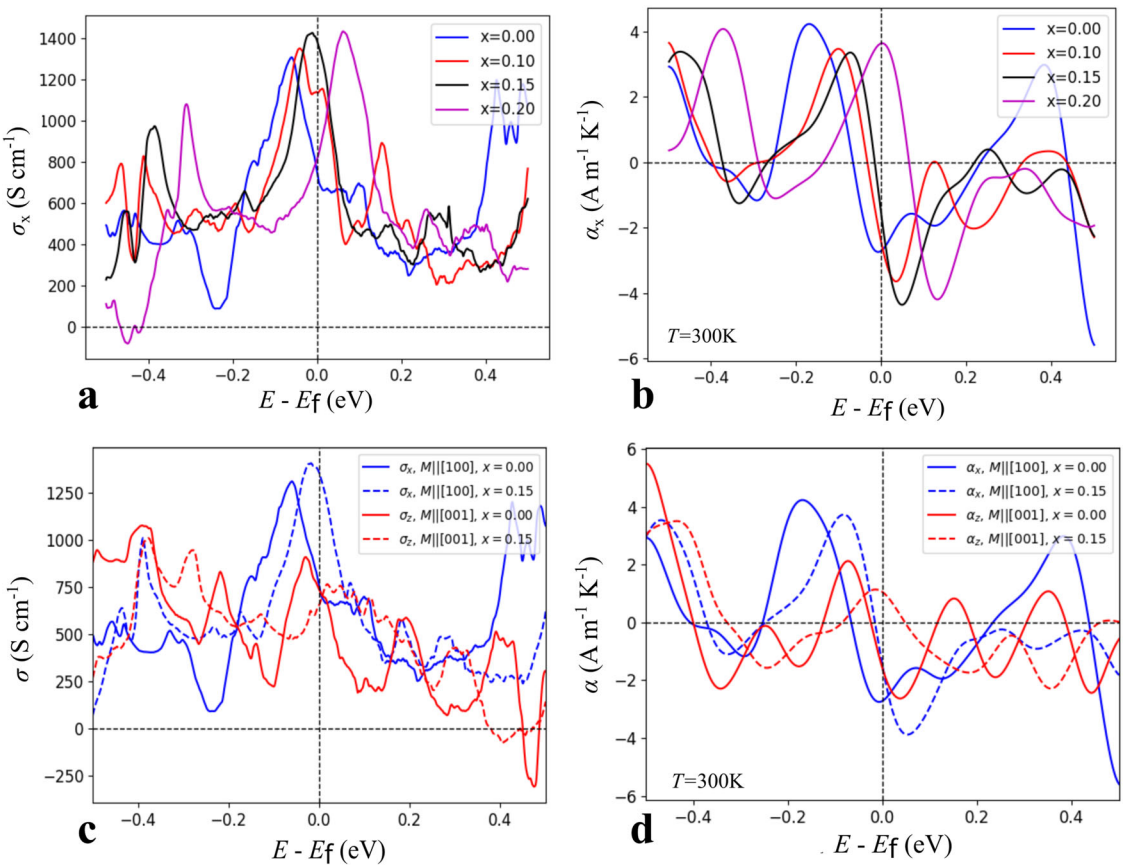

Fig. 5 Tunability of anomalous Hall and Nernst conductivities in respect to strain and magnetization direction for Fe_3Sn. a The x-component ($\sigma_x = \sigma_{yz}$) of the full AHC as a function of energy for different doping concentrations x of $(Fe_{1-x}Mn_x)_3Sn$. **b** The x-component ($\alpha_x = \alpha_{yz}$) of the full ANC as a function of energy for different doping concentrations x of $(Fe_{1-x}Mn_x)_3Sn$. **c** AHC as a function of energy for different magnetization directions and doping concentrations of $(Fe_{1-x}Mn_x)_3Sn$. **d** ANC as a function of energy for different magnetization directions and concentrations of $(Fe_{1-x}Mn_x)_3Sn$.

the Fermi level to match the position of the peak is doable by means of doping. In order to investigate this possibility, we consider $(Fe_{1-x}Mn_x)_3Sn$ for various values of x, with $x \in [0, 0.2]$, indicating the percentage of Mn doping to the system. By using virtual crystal approximation (VCA) calculations, we compute the AHC curve for different x, as illustrated in Fig. 5a. It is noted that the position of the peak approaches the Fermi level while the Mn dopand concentration is increased and it hits the Fermi energy at approximately $x = 0.15$ (black curve). The existence of the AHC peak and its location affects the calculated ANC. While the energy of the peak is lower than the Fermi energy ($x < 0.15$), the ANC is gradually decreased from -2.71 A m^{-1} K^{-1} for $x = 0$ to -1.58 A m^{-1} K^{-1} for $x = 0.15$. Once the energy of the peak gets larger than the Fermi energy ($x > 0.15$), ANC changes sign and jumps to 3.63 A m^{-1} K^{-1} for $x = 0.2$. Figure 5b shows the calculated ANC curves for various x, demonstrating that Fe_3Sn offers an interesting playground of controlling the ANC by doping even with a sign change.

Since $(Fe_{0.85}Mn_{0.15})_3Sn$ exhibits the closest peak to the Fermi energy, its dynamical stability was checked by calculating its phonon dispersion (see Supplementary Fig. 3). To mimic the disorder structure, $(Fe_{0.85}Mn_{0.15})_3Sn$, a supercell, containing 80 atoms in special quasi-random structure (SQS)[73], was generated by the mcsqs code of the ATAT package[74]. As illustrated in Supplementary Fig. 3, the absence of imaginary modes indicates $(Fe_{0.85}Mn_{0.15})_3Sn$ is dynamically stable.

Tuning the magnetization direction allows easier ANC modifications. In an attempt to tune the AHC and ANC of Fe_3Sn, we considered different magnetization directions i.e., along [100], [010], and [001] axes. Our results show no impact of the magnetization direction to the AHC and ANC values along [100] and [010] axis, where the values remain practically unchanged at 757 S cm^{-1} and -2.58 A m^{-1} K^{-1} due to the underlying hexagonal symmetry. On the other hand, a small change is noticed for direction along [001], where the AHC (ANC) is tuned to 676 S cm^{-1} (-2.06 A m^{-1} K^{-1}), see Fig. 5c and d (solid curves). Despite the minor changes in the AHC and ANC values at Fermi energy, a larger impact of the altering of the magnetization direction is observed away from the charge-neutral point for both magnetization directions and doping concentrations (solid and dashed curves, respectively). Specifically, the AHC peak of 1308 S cm^{-1} at 60 meV below the Fermi energy is moved closer to the Fermi energy, at 35 meV below the Fermi energy, and further reduces its maximum value to 886 S cm^{-1} when the magnetization direction is along the [001]-axis. The outcome of this change is more obvious in the ANC, where the zero value of the [001] direction is located closer to the Fermi energy, being useful for future applications. It is finally noted that for M||[001], doping results in ANC sign change (Fig. 5d, red curves).

Based on DFT calculations, the thermodynamical properties of the Fe–Sn system and the topological transport properties of Fe_3Sn are studied. Thermodynamic modeling of the Fe–Sn phase diagram has been re-established. The problems concerning

invariant reactions of intermetallics are remedied under our newly measured temperature ranges. First-principles phonon calculations with the QHA approach were performed to calculate the thermodynamic properties at finite temperatures. Thermodynamic properties, phonon dispersions of pure elements, and intermetallics were predicted to make up the shortage of experimental data. A set of self-consistent thermodynamic parameters are obtained by the CALPHAD approach. Further, we evaluated the AHC and ANC of Fe_3Sn with magnetization direction and doping being perturbations. The calculated AHC of 757 S cm^{-1} is the largest among all reported members of the Fe–Sn family. It is noted that the nodal lines combined with the extended small gap areas constitute the main contribution to the total AHC and they can further be tuned by doping Mn at the Fe sites, allowing the manipulation of the AHC and ANC values and offering good candidate materials for promising transverse thermoelectric devices. In addition, promising high-throughput calculations[75,76] can be performed to search for more intriguing magnetic intermetallic compounds with singular topological transport properties, assisted by automated Wannier function construction[77] for transport property calculations.

METHODS

First-principles calculations

Our calculations were performed using the generalized gradient approximation (GGA) for the exchange-correlation functional, in the parameterization of Perdew–Burke–Ernzerhof[78] for the Vienna ab initio Simulation Package (VASP)[79,80]. The energy cutoff is set at 600 eV and at least 5000 k-points in the first Brillouin zone with Γ-centered k-mesh were used for the hexagonal lattices (Fe_3Sn, FeSn, and Fe_5Sn_3), while for all the other structures, Monkhorst–Pack grids were used. The energy convergence criterion was set as 10^{-6} eV, and 10^{-5} eV Å^{-1} was set as the tolerance of forces during the structure relaxation. The enthalpy of formation, $\Delta_f H(Fe_xSn_y)$, for the Fe_xSn_y intermetallic compounds was obtained following

$$\Delta_f H(Fe_xSn_y) = E_{Fe_{xSny}} - \frac{x}{x+y}E_{Fe} - \frac{y}{x+y}E_{Sn}, \quad (4)$$

where all the total energies for the equilibrium phases in their corresponding stable structures were obtained after structural relaxation.

For the phonon calculations, the frozen phonon approach was applied using the PHONOPY package[80]. The temperature-dependent thermodynamical properties were calculated by using the quasi-harmonic approximation[81]. The Gibbs free energy $G(T, P)$ at temperature T and pressure P can be obtained from the Helmholtz free energy $F(T, V)$ as follows[82]:

$$G(P,T) - PV = F(T,V) = E_0(V) + F_{vib}(V,T) + F_{el}(V,T) + F_{magn}(V,T), \quad (5)$$

where E_0(V) is the total energy at zero Kelvin without the zero-point energy contribution, which were determined by fitting of the energies with respect to the volume data using the Birch–Murnaghan equation of state (EOS)[83]. F_{vib} corresponds to the lattice vibration contribution to the Helmholtz energy, which can be derived from the phonon density of states (PhDOS), $g(\omega, V)$, by using the following equation[82]:

$$F_{vib}(V,T) = k_B T \int_0^\infty \left[2\sinh\frac{\hbar\omega}{2k_BT}\right] g(\omega,V)\mathrm{d}\omega, \quad (6)$$

where k_B and $\hbar$ are the Boltzmann constant and reduced Planck constant, respectively, and ω denotes the phonon frequency for a given wave vector **q**. The PhDOS $g(\omega, V)$ can be obtained by integrating the phonon dispersion in the Brillouin zone. The third term F_{el} represents the electronic contribution to the Helmholtz free energy, obtained by[84]:

$$F_{el}(V,T) = E_{el}(V,T) - T \cdot S_{el}(V,T) \quad (7)$$

where $E_{el}(V, T)$ and $S_{el}(V, T)$ indicate the electronic energy and electronic entropy, respectively. With the electronic DOS, both terms can be formulated as[84]:

$$E_{el}(V,T) = \int n(\epsilon) f \epsilon \mathrm{d}\epsilon - \int_{-\infty}^{\epsilon_F} n(\epsilon, V)\mathrm{d}\epsilon, \quad (8)$$

$$S_{el}(V,T) = -k_B \int n\epsilon[f\ln f + (1-f)\ln(1-f)]\mathrm{d}\epsilon, \quad (9)$$

where $n(\epsilon)$ is the electronic DOS, f represents the Fermi-Dirac distribution function and ϵ_F is the Fermi energy.

Finally, based on the original Inden–Hillert–Jarl (IHJ) model[38,39] and further improved expression by Xiong[40], the magnetic Gibbs energy can be formulated as:

$$G_{magn} = RT(\beta^* + 1)f(\tau), \quad (10)$$

where τ is T/T^*, T^* is the critical temperature (the Cutie temperature T_C for ferromagnetic materials or the Neel temperature T_N for antiferromagnetic materials). β^* is the effective magnetic moment per atom[40]. And the relative parameters are summarized in Supplementary Table 2. Note that, we adopted the experimental critical temperatures and calculated magnetic moments.

In order to evaluate AHC, we projected the Bloch wave functions onto maximally localized wannier functions (MLWF) using Wannier90, following ref. [85]. A total number of 124 MLWFs, originating from the *s*, *p* and *d* orbitals of Fe atoms and the s and p orbitals of Sn atoms, are used. AHC is obtained by integrating the Berry curvature according to the formula:

$$\sigma_{\alpha\beta} = -\frac{e^2}{\hbar}\int \frac{\mathbf{dk}}{(2\pi)^3}\sum f[\epsilon(\mathbf{k}) - \mu]\Omega_{n,\alpha\beta}(\mathbf{k}),$$
$$\Omega_{n,\alpha\beta}(\mathbf{k}) = -2\mathrm{Im}\sum_{m\neq n}\frac{\langle \mathbf{k}n|v_\alpha|\mathbf{k}m\rangle\langle \mathbf{k}m|v_\beta|\mathbf{k}n\rangle}{[\epsilon_m(\mathbf{k}) - \epsilon_n(\mathbf{k})]^2}, \quad (11)$$

with μ, f, n, m, $\epsilon_n(\mathbf{k})$, $\epsilon_m(\mathbf{k})$, and v_α being the Fermi level, the Fermi-Dirac distribution function, the occupied Bloch band, the empty Bloch band, their corresponding energy eigenvalues and the Cartesian component of the velocity operator. The integration is performed on a $270 \times 270 \times 350$ mesh using Wanniertools[86]. ANC is evaluated using an in-house developed Python script, following the formula:

$$a_{\alpha\beta} = -\frac{1}{e}\int \mathrm{d}\epsilon \frac{\partial f}{\partial \mu}\sigma_{\alpha\beta}(\epsilon)\frac{\epsilon - \mu}{T} \quad (12)$$

where T, e, and ϵ are the temperature, the electronic charge and the energy point within the integration energy window, respectively. An energy grid of 1000 points within the window $[-0.5, 0.5]$eV with respect to the Fermi level was chosen.

Mn doping at Fe sites is performed by using the virtual crystal approximation (VCA)[87] as implemented in VASP[88,89]. In this approximation, virtual, fictitious atoms that behave in between the parent atoms are inserted. VCA techniques have been used to describe prototypical doped $\gamma - FeMn$ systems[90] and magnetic anisotropy energy of $L1_0FePt$ and $Fe_{1-x}Mn_xPt$[91] and additionally topological transport properties of $Co_{3-x}Ni_xSn_2S_2$[92] and Fe_3Co alloys[93].

CALPHAD modeling

Pure elements. The Gibbs free energies for pure Fe and Sn were taken from the Scientific Group Thermodata Europe (SGTE) pure element database[94], which was described by:

$${}^{\circ}G_i^{\phi}(T) = G_i^{\phi}(T) - H_{i,SER}(298.15\,K) = a + bT + cT(T) + dT^2 + eT^3 + fT^{-1} + gT^7 + hT^{-9}, \quad (13)$$

where i represents the pure elements Fe or Sn, $H_{i,\mathrm{SER}}(298.15K)$ is the molar enthalpy of element i at 298.15 K in its standard element reference (SER) state, and a to h are known coefficients.

Solution phases. The solution phases, Liquid, BCC_A2, FCC_A1 and BCT_A5 phases are described using the substitutional solution model, with the corresponding molar Gibbs free energy formulated as:

$$G_m^{\varphi} = x_{\mathrm{Fe}} G_{\mathrm{Fe}}^{\varphi}(T) + x_{\mathrm{Sn}} G_{\mathrm{Sn}}^{\varphi}(T) + RT(x_{\mathrm{Fe}} x_{\mathrm{Fe}} + x_{Sn} x_{\mathrm{Sn}}) + G^{ex} + G^{\mathrm{magn}}, \tag{14}$$

where x_{Fe} and x_{Sn} are the mole fraction of Fe and Sn in the solution, respectively. Taken from SGTE[94], G_i^{φ} denotes the molar Gibbs free energy of pure Fe and Y in the structure φ at the given temperature. G^{ex} denotes the excess Gibbs energy of mixing, which measures the deviation of the actual solution from the ideal solution behavior, modeled using a Redlich–Kister polynomial[95]:

$$G^{ex} = x_{\mathrm{Fe}} x_{\mathrm{Sn}} \sum_{j=0}^{n} {}^{(j)}L_{\mathrm{Fe,Sn}}^{\varphi}(x_{\mathrm{Fe}} - x_{\mathrm{Sn}})^j. \tag{15}$$

The jth interaction parameter between Fe and Sn is described by ${}^{(j)}\mathrm{L}_{\mathrm{Fe,Sn}}^{\varphi}$, which is modeled in terms of a^*+b^*T.

Stoichiometric intermetallic compounds. Fe_5Sn_3, Fe_3Sn_2, Fe_3Sn, FeSn, and $FeSn_2$ were considered as stoichiometric phases. The Gibbs free energies per mole atom of these phases were thus expressed as follows:

$$G_m^{\mathrm{Fe_{xSny}}} = \frac{x}{x+y} G_{\mathrm{Fe,SER}} + \frac{y}{x+y} G_{\mathrm{Sn,SER}} + \Delta G_f^{\mathrm{Fe_{xSny}}}(T), \tag{16}$$

where $\Delta G_f^{\mathrm{Fe_{xSny}}}(T)$ is the Gibbs free energy of formation of the stoichiometric compound Fe_xSn_y which can be expressed as:

$$\Delta G_f^{\mathrm{Fe_{xSny}}}(T) = A_3 + B_3 T, \tag{17}$$

where the coefficients A_3, B_3 are the parameters to be optimized. Since there is no experimental data of the thermodynamic properties for such intermetallic phases, the calculated enthalpies of formation for these phases from DFT calculations were treated as initial values of the coefficient A_3 in Eq. (17) in the present optimization.

DATA AVAILABILITY

The authors declare that the code supporting this study is available on GitHub under the link https://github.com/TMM-TUDA/Automatic-wannier-flow.

Received: 29 March 2022; Accepted: 20 October 2022;
Published online: 01 December 2022

REFERENCES

1. Yin, J.-X. et al. Giant and anisotropic many-body spin–orbit tunability in a strongly correlated Kagome magnet. *Nature* **562**, 91–95 (2018).
2. Fenner, L., Dee, A. & Wills, A. Non-collinearity and spin frustration in the itinerant Kagome ferromagnet Fe_3Sn_2. *J. Condens. Matter Phys.* **21**, 452202 (2009).
3. Mekata, M. Kagome: the story of the basketweave lattice. *Phys. Today* **56**, 12 (2003).
4. Zhou, Y., Kanoda, K. & Ng, T.-K. Quantum spin liquid states. *Rev. Mod. Phys.* **89**, 025003 (2017).
5. Ohgushi, K., Murakami, S. & Nagaosa, N. Spin anisotropy and quantum Hall effect in the Kagomé lattice: chiral spin state based on a ferromagnet. *Phys. Rev. B* **62**, R6065 (2000).
6. Yan, S., Huse, D. A. & White, S. R. Spin-liquid ground state of the S= 1/2 Kagome Heisenberg antiferromagnet. *Science* **332**, 1173–1176 (2011).
7. Han, T.-H. et al. Fractionalized excitations in the spin-liquid state of a Kagome-lattice antiferromagnet. *Nature* **492**, 406–410 (2012).
8. Mazin, I. et al. Theoretical prediction of a strongly correlated Dirac metal. *Nat. Commun.* **5**, 1–7 (2014).
9. Chisnell, R. et al. Topological magnon bands in a Kagome lattice ferromagnet. *Phys. Rev. Lett.* **115**, 147201 (2015).
10. Xu, G., Lian, B. & Zhang, S.-C. Intrinsic quantum anomalous Hall effect in the Kagome lattice $Cs_2LiMn_3F_{12}$. *Phys. Rev. Lett.* **115**, 186802 (2015).
11. Zhu, W., Gong, S.-S., Zeng, T.-S., Fu, L. & Sheng, D. Interaction-driven spontaneous quantum Hall effect on a Kagome lattice. *Phys. Rev. Lett.* **117**, 096402 (2016).
12. Guo, H.-M. & Franz, M. Topological insulator on the Kagome lattice. *Phys. Rev. B* **80**, 113102 (2009).
13. Xu, G., Weng, H., Wang, Z., Dai, X. & Fang, Z. Chern semimetal and the quantized anomalous Hall effect in $HgCr_2Se_4$. *Phys. Rev. Lett.* **107**, 186806 (2011).
14. Chen, H., Niu, Q. & MacDonald, A. H. Anomalous Hall effect arising from noncollinear antiferromagnetism. *Phys. Rev. Lett.* **112**, 017205 (2014).
15. Kübler, J. & Felser, C. Non-collinear antiferromagnets and the anomalous Hall effect. *EPL (Europhys. Lett.)* **108**, 67001 (2014).
16. Tang, E., Mei, J.-W. & Wen, X.-G. High-temperature fractional quantum Hall states. *Phys. Rev. Lett.* **106**, 236802 (2011).
17. Kane, C. L. & Mele, E. J. Quantum spin Hall effect in graphene. *Phys. Rev. Lett.* **95**, 226801 (2005).
18. Bernevig, B. A., Felser, C. & Beidenkopf, H. Progress and prospects in magnetic topological materials. *Nature* **603**, 41–51 (2022).
19. Giefers, H. & Nicol, M. High pressure x-ray diffraction study of all Fe–Sn intermetallic compounds and one Fe–Sn solid solution. *J. Alloy. Compd.* **422**, 132–144 (2006).
20. Häggström, L., Ericsson, T. & Wäppling, R. An investigation of CoSn using Mössbauer spectroscopy. *Phys. Scr.* **11**, 94 (1975).
21. Kang, M. et al. Dirac fermions and flat bands in the ideal Kagome metal FeSn. *Nat. Mater.* **19**, 163–169 (2020).
22. Lin, Z. et al. Flatbands and emergent ferromagnetic ordering in Fe_3Sn_2 Kagome lattices. *Phys. Rev. Lett.* **121**, 096401 (2018).
23. Lin, Z.-Z. & Chen, X. Tunable massive Dirac fermions in ferromagnetic Fe_3Sn_2 Kagome lattice. *Phys. Status Solidi-R.* **14**, 1900705 (2020).
24. Lin, Z. et al. Dirac fermions in antiferromagnetic FeSn Kagome lattices with combined space inversion and time-reversal symmetry. *Phys. Rev. B* **102**, 155103 (2020).
25. Wang, Q. et al. Anomalous Hall effect in a ferromagnetic Fe_3Sn_2 single crystal with a geometrically frustrated Fe bilayer Kagome lattice. *Phys. Rev. B* **94**, 075135 (2016).
26. Tanaka, H. et al. Three-dimensional electronic structure in ferromagnetic Fe_3Sn_2 with breathing Kagome bilayers. *Phys. Rev. B* **101**, 161114 (2020).
27. Li, H. et al. Large topological Hall effect in a geometrically frustrated Kagome magnet Fe_3Sn_2. *Appl. Phys. Lett.* **114**, 192408 (2019).
28. Kida, T. et al. The giant anomalous Hall effect in the ferromagnet Fe_3Sn_2—a frustrated Kagome metal. *J. Condens. Matter Phys.* **23**, 112205 (2011).
29. Li, H. et al. Large anomalous Hall effect in a hexagonal ferromagnetic Fe_5Sn_3 single crystal. *Phys. Rev. B* **101**, 140409 (2020).
30. Zhang, H., Xu, C. & Ke, X. Topological Nernst effect, anomalous Nernst effect, and anomalous thermal Hall effect in the Dirac semimetal Fe_3Sn_2. *Phys. Rev. B* **103**, L201101 (2021).
31. Sales, B. C. et al. Electronic, magnetic, and thermodynamic properties of the Kagome layer compound FeSn. *Phys. Rev. Mater.* **3**, 114203 (2019).
32. Fayyazi, B. et al. Bulk combinatorial analysis for searching new rare-earth free permanent magnets: reactive crucible melting applied to the Fe-Sn binary system. *Acta Mater.* **141**, 434–443 (2017).
33. Fayyazi, B. et al. Experimental and computational analysis of binary Fe-Sn ferromagnetic compounds. *Acta Mater.* **180**, 126–140 (2019).
34. Tréheux, D. & Guiraldenq, P. Etude des diagrammes d'equilibre binaires par la methode des couples de diffusion. application au systeme fer-etain. *Scr. Mater.* **8**, 363–366 (1974).
35. Kumar, K. H., Wollants, P. & Delaey, L. Thermodynamic evaluation of Fe-Sn phase diagram. *Calphad* **20**, 139–149 (1996).
36. Brockhouse, B., Abou-Helal, H. & Hallman, E. Lattice vibrations in iron at 296 K. *Solid State Commun.* **5**, 211–216 (1967).
37. Wallace, D., Sidles, P. & Danielson, G. Specific heat of high purity iron by a pulse heating method. *J. Appl. Phys.* **31**, 168–176 (1960).
38. Inden, G. Approximate description of the configurational specific heat during a magnetic order-disorder transformation. in *Proceeding of the 5th Project Meeting CALPHAD*, Elsevier, Vol. 3, 4–1 (1976).
39. Hillert, M. & Jarl, M. A model for alloying in ferromagnetic metals. *Calphad* **2**, 227–238 (1978).
40. Xiong, W., Chen, Q., Korzhavyi, P. A. & Selleby, M. An improved magnetic model for thermodynamic modeling. *Calphad* **39**, 11–20 (2012).

41. Sundman, B., Lukas, H. & Fries, S. *Computational Thermodynamics: The Calphad Method* (Cambridge University Press, 2007).
42. Sundman, B., Jansson, B. & Andersson, J.-O. The thermo-calc databank system. *Calphad* **9**, 153–190 (1985).
43. Fan, L., Shen, C., Hu, K., Liu, H. & Zhang, H. DFT calculations and thermodynamic re-assessment of the Fe-Y binary system. *J. Phase Equilib. Diff.* **42**, 348–362 (2021).
44. Shen, C., Hu, K., Fan, L. & Zhang, H. Thermodynamic reassessment of the Au-In binary system supported with first-principles calculations. *J. Phase Equilib. Diff.* **42**, 479–488 (2021).
45. Edwards, C. & Preece, A. A study of the constitution of the iron-tin alloys. *J. Iron Steel Inst. Lond.* **124**, 41–69 (1931).
46. Mills, K. & Turkdogan, E. Liquid miscibility gap in iron-tin system. *Trans. Metall. Soc. Aime.* **230**, 1202 (1964).
47. Kubaschewski, O. *Iron-Binary Phase Diagrams* (Springer Science & Business Media, 2016).
48. Isaac, E. & Tammann, G. On the alloys of iron with tin and gold. *Z. Anorg. Chem.* **53**, 281 (1907).
49. Fedorenko, A. & Brovkin, V. Vapor pressure of tin and thermodynamic properties of the tin–iron system. *Sb. Nauchn. Tr. –Gos. Proektn. Nauchno-Issled. Inst. Gipronikel* **3**, 83–89 (1977).
50. Treheux, D., Duc, D. & Guiraldenq, P. Determination of the solubility limits of Sn in the alpha and gamma phases of Fe. *Mem. Sci. Rev. Met.* **71**, 289–293 (1974).
51. Singh, M. & Bhan, S. Contribution to the Fe-Sn system. *J. Mater. Sci. Lett.* **5**, 733–735 (1986).
52. Nunoue, S. & Kato, E. Mass spectrometric determination of the miscibility gap in the liquid Fe-Sn system and the activities of this system at 1550 °C and 1600°C. *Tetsu-to-Hagané* **73**, 868–875 (1987).
53. Arita, M., Ohyama, M., Goto, K. & Someno, M. Measurements of activity, solubility, and diffusivity in *α* and *γ* iron-tin alloys between 1183 and 1680 K. *Int. J. Mater. Res.* **12**, 244–250 (1981).
54. Okamoto, H. et al. *Binary Alloy Phase Diagrams* (ASM International, Materials Park, 1990).
55. Yamamoto, T., Takashima, T. & Nishida, K. Inter-diffusion in the alpha-solid solution of the Fe-Sn system. *J. Jpn. Inst. Met.* **45**, 985–990 (1981).
56. Jannin, C., Michel, A. & Lecocq, P. Magnetism and properties of different phases in the Fe-Sn system. *Comptes Redus Hebomadaires Seances Acad. Sci.* **257**, 1906–1907 (1963).
57. Huang, Y.-C., Gierlotka, W. & Chen, S.-W. Sn–Bi–Fe thermodynamic modeling and Sn–Bi/Fe interfacial reactions. *Intermetallics* **18**, 984–991 (2010).
58. Ye, L. et al. Massive Dirac fermions in a ferromagnetic Kagome metal. *Nature* **555**, 638–642 (2018).
59. Chen, D. et al. Large anomalous Hall effect in the Kagome ferromagnet $LiMn_6Sn_6$. *Phys. Rev. B* **103**, 144410 (2021).
60. Asaba, T. et al. Anomalous Hall effect in the Kagome ferrimagnet $GdMn_6Sn_6$. *Phys. Rev. B* **101**, 174415 (2020).
61. Liu, E. et al. Giant anomalous Hall effect in a ferromagnetic Kagome-lattice semimetal. *Nat. Phys.* **14**, 1125–1131 (2018).
62. Samathrakis, I., Long, T., Zhang, Z., Singh, H. K. & Zhang, H. Enhanced anomalous Nernst effects in ferromagnetic materials driven by Weyl nodes. *J. Phys. D: Appl. Phys.* **55**, 074003 (2021).
63. Yang, H. et al. Giant anomalous Nernst effect in the magnetic Weyl semimetal $Co_3Sn_2S_2$. *Phys. Rev. Mater.* **4**, 024202 (2020).
64. Zhou, W. et al. Seebeck-driven transverse thermoelectric generation. *Nat. Mater.* **20**, 463–467 (2021).
65. Uchida, K.-i, Zhou, W. & Sakuraba, Y. Transverse thermoelectric generation using magnetic materials. *Appl. Phys. Lett.* **118**, 140504 (2021).
66. Sakai, A. et al. Iron-based binary ferromagnets for transverse thermoelectric conversion. *Nature* **581**, 53–57 (2020).
67. Yamamoto, K. et al. Phenomenological analysis of transverse thermoelectric generation and cooling performance in magnetic/thermoelectric hybrid systems. *J. Appl. Phys.* **129**, 223908 (2021).
68. Seemann, M., Ködderitzsch, D., Wimmer, S. & Ebert, H. Symmetry-imposed shape of linear response tensors. *Phys. Rev. B* **92**, 155138 (2015).
69. Suzuki, M.-T., Koretsune, T., Ochi, M. & Arita, R. Cluster multipole theory for anomalous Hall effect in antiferromagnets. *Phys. Rev. B* **95**, 094406 (2017).
70. Nagaosa, N., Sinova, J., Onoda, S., MacDonald, A. H. & Ong, N. P. Anomalous Hall effect. *Rev. Mod. Phys.* **82**, 1539 (2010).
71. Xu, Y. et al. High-throughput calculations of magnetic topological materials. *Nature* **586**, 702–707 (2020).
72. Singh, H. K. et al. Multifunctional antiperovskites driven by strong magnetostructural coupling. *npj Comput. Mater.* **7**, 1–9 (2021).
73. Zunger, A., Wei, S.-H., Ferreira, L. & Bernard, J. E. Special quasirandom structures. *Phys. Rev. Lett.* **65**, 353 (1990).
74. Van de Walle, A. et al. Efficient stochastic generation of special quasirandom structures. *Calphad* **42**, 13–18 (2013).
75. Zhang, H. High-throughput design of magnetic materials. *Electron. Struct.* **3**, 033001 (2021).
76. Shen, C. et al. Designing of magnetic MAB phases for energy applications. *J. Mater. Chem. A* **9**, 8805–8813 (2021).
77. Zhang, Z. et al. High-throughput screening and automated processing toward novel topological insulators. *J. Phys. Chem. Lett.* **9**, 6224–6231 (2018).
78. Perdew, J. P., Burke, K. & Ernzerhof, M. Generalized gradient approximation made simple. *Phys. Rev. Lett.* **77**, 3865 (1996).
79. Kresse, G. & Furthmüller, J. Efficiency of ab-initio total energy calculations for metals and semiconductors using a plane-wave basis set. *Comput. Mater. Sci.* **6**, 15–50 (1996).
80. Togo, A. & Tanaka, I. First principles phonon calculations in materials science. *Scr. Mater.* **108**, 1–5 (2015).
81. Baroni, S., Giannozzi, P. & Isaev, E. Density-functional perturbation theory for quasi-harmonic calculations. *Rev. Mineral. Geochem.* **71**, 39–57 (2010).
82. Hu, Y. et al. First-principles calculations and thermodynamic modeling of the Yb-Ni binary system. *Calphad* **59**, 207–217 (2017).
83. Wang, Y., Liu, Z. & Chen, L. Thermodynamic properties of Al, Ni, NiAl, and Ni_3Al from first-principles calculations. *Acta Mater.* **52**, 2665–2671 (2004).
84. Liang, S., Singh, H., Zhang, H. & Schmid-Fetzer, R. Phase equilibria of the Zn-Ti system: experiments, first-principles calculations and Calphad assessment. *Calphad* **64**, 213–224 (2019).
85. Mostofi, A. A. et al. wannier90: a tool for obtaining maximally-localised wannier functions. *Comput. Phys. Commun.* **178**, 685 – 699 (2008).
86. Wu, Q., Zhang, S., Song, H.-F., Troyer, M. & Soluyanov, A. A. Wanniertools: an open-source software package for novel topological materials. *Comput. Phys. Commun.* **224**, 405–416 (2018).
87. Bellaiche, L. & Vanderbilt, D. Virtual crystal approximation revisited: application to dielectric and piezoelectric properties of perovskites. *Phys. Rev. B* **61**, 7877 (2000).
88. Eckhardt, C., Hummer, K. & Kresse, G. Indirect-to-direct gap transition in strained and unstrained Sn_xGe_{1-x} alloys. *Phys. Rev. B* **89**, 165201 (2014).
89. Steiner, S., Khmelevskyi, S., Marsmann, M. & Kresse, G. Calculation of the magnetic anisotropy with projected-augmented-wave methodology and the case study of disordered $Fe_{1-x}Co_x$ alloys. *Phys. Rev. B* **93**, 224425 (2016).
90. Hanke, J.-P., Freimuth, F., Blügel, S. & Mokrousov, Y. Prototypical topological orbital ferromagnet *γ*-FeMn. *Sci. Rep.* **7**, 1–7 (2017).
91. Burkert, T. et al. Magnetic anisotropy of $L1_0$ FePt and $Fe_{1-x}Mn_xPt$. *Phys. Rev. B* **71**, 134411 (2005).
92. Shen, J. et al. Local disorder-induced elevation of intrinsic anomalous Hall conductance in an electron-doped magnetic Weyl semimetal. *Phys. Rev. Lett.* **125**, 086602 (2020).
93. Bianco, R., Resta, R. & Souza, I. How disorder affects the berry-phase anomalous Hall conductivity: a reciprocal-space analysis. *Phys. Rev. B* **90**, 125153 (2014).
94. Dinsdale, A. SGTE data for pure elements. *Calphad* **15**, 317–425 (1991).
95. Redlich, O. & Kister, A. Algebraic representation of thermodynamic properties and the classification of solutions. *Ind. Eng. Chem. Res.* **40**, 345–348 (1948).

ACKNOWLEDGEMENTS

This work was funded by the Deutsche Forschungsgemeinschaft (DFG, German Research Foundation) - Project-IDs 405553726 - TRR 270 and 443703006 - CRC 1487 Iron, upgraded.Calculations for this research were conducted on the Lichtenberg high performance computer of TU Darmstadt. Kun Hu acknowledges the financial support from the China Scholarship Council (CSC).

AUTHOR CONTRIBUTIONS

C.S. and K.H. performed all CALPHAD assessments and calculations related to the thermodynamical properties. I.S. performed all calculations related to the topological transport properties. C.S. and I.S. wrote the manuscript. C.S., K.H., and N.F. were involved in the discussions related to the results of the thermodynamical properties. I.S. and H.K.S. were involved in the discussions related to the results of the topological transport properties. H.L., O.G., and H.Z. supervised by providing useful guidance, comments, and suggestions.

FUNDING

Open Access funding enabled and organized by Projekt DEAL.

COMPETING INTERESTS

The authors declare no competing interests.

ADDITIONAL INFORMATION

Supplementary information The online version contains supplementary material available at https://doi.org/10.1038/s41524-022-00917-1.

Correspondence and requests for materials should be addressed to Kun Hu or Hongbin Zhang.

Reprints and permission information is available at http://www.nature.com/reprints

Publisher's note Springer Nature remains neutral with regard to jurisdictional claims in published maps and institutional affiliations.

Open Access This article is licensed under a Creative Commons Attribution 4.0 International License, which permits use, sharing, adaptation, distribution and reproduction in any medium or format, as long as you give appropriate credit to the original author(s) and the source, provide a link to the Creative Commons license, and indicate if changes were made. The images or other third party material in this article are included in the article's Creative Commons license, unless indicated otherwise in a credit line to the material. If material is not included in the article's Creative Commons license and your intended use is not permitted by statutory regulation or exceeds the permitted use, you will need to obtain permission directly from the copyright holder. To view a copy of this license, visit http://creativecommons.org/licenses/by/4.0/.

© The Author(s) 2022